Journal of Materials Processing Tech. 348 (2026) 119178

Contents lists available at ScienceDirect

Journal of Materials Processing Tech.

journal homepage: www.elsevier.com/locate/jmatprotec

Research article

Cold manufacturing of metallic glass-based composites by ultrasonic vibrations

Luyao Li [a,b], Yu Zhang [b], Jinbiao Huang [b], Zhe Chen [b], Xiangyang Yu [b], Wei Li [a], Jiasen Sun [b], Kangyu Lin [b], Chenchen Yuan [a,*], Jiang Ma [b,c,d,**]

[a] School of Materials Science and Engineering, Jiangsu Key Laboratory for Advanced Metallic Materials, Southeast University, Nanjing 211189, China
[b] Shenzhen Key Laboratory of High Performance Nontraditional Manufacturing, College of Mechatronics and Control Engineering, Shenzhen University, Shenzhen 518060, China
[c] Guangdong Provincial Key Laboratory of Micro/Nano Optomechatronics Engineering, Shenzhen University, Shenzhen 518060, China
[d] State Key Laboratory of Radio Frequency Heterogeneous Integration, Shenzhen University, Shenzhen 518060, China

ARTICLE INFO

Keywords:
Composite materials
Cold manufacturing
Metallic glasses
Ultrasonic Vibration

ABSTRACT

The design of materials with desirable and tailorable properties is a long-standing goal within materials science, where composites represent a key strategy. However, a central dilemma in conventional composite manufacturing is that the thermal energy required to form strong interfacial bonds often simultaneously induces detrimental side effects, including interfacial reactions and reinforcement degradation. To resolve this generic conflict, we introduce a versatile "cold manufacturing" strategy utilizing metallic glasses as matrices. By exploiting an athermal ultrasonic vibration mechanism—which induces transient liquid-like behavior in metallic glasses without thermal activation—we achieve seamless interfacial bonding across diverse conductors, insulators, metals, and non-metals via oxide-layer-penetrating diffusion at ambient conditions. Crucially, successful fabrication underwater and in liquid nitrogen definitively demonstrates the technique's purely athermal nature, avoiding any thermal degradation pathways. By tuning metallic glasses binder ratios and additive compositions, we precisely engineer mechanical properties (Vickers hardness: 400–1450 HV) and magnetic response (saturation magnetization: 0–158.6 emu/g), forming robust bonds. This work thus establishes a versatile and fundamentally distinct composite manufacturing platform, opening a generic pathway to multifunctional composites free from the intrinsic limitations of heat.

1. Introduction

Materials have fundamentally shaped the trajectory of human civilization, as intuitively reflected in the nomenclature of historical epochs—from the Stone Age and Bronze Age to the Iron Age, culminating in today's "Silicon Age" [1]. The material domain is vast and diverse, characterized by rich functionalities, while societal demand for advanced materials continues to escalate, intensifying the pressure to develop novel alternatives. This relentless pursuit has driven the development of composite materials, which combine two or more distinct phases to achieve synergistic properties unattainable by their individual constituents [2,3]. Polymer matrix [4] and ceramic matrix [5] composites— the primary focus of these prior studies—struggle to simultaneously achieve high strength, ductility and temperature stability, creating an urgent need for metal-matrix composites (MMC). However, while metals exhibit outstanding mechanical properties, their inherent high melting points lead to poor adhesion, impeding their utility as composite matrix. While prior studies suggest that metal-matrix composites could integrate high specific strength [6], superior thermal conductivity [7], and elevated-temperature stability [8], their practical translation has been hindered by unresolved fabrication bottlenecks—underscoring the need for innovative manufacturing strategies to unlock MMC's full potential.

Nevertheless, existing MMC fabrication techniques—whether liquid-state (stir casting [9], melt infiltration [10]), deposition-based [11], or solid-state (powder metallurgy [12], diffusion bonding [13])—share a

* Corresponding author.
** Corresponding author at: Shenzhen Key Laboratory of High Performance Nontraditional Manufacturing, College of Mechatronics and Control Engineering, Shenzhen University, Shenzhen 518060, China.
E-mail addresses: yuancc@seu.edu.cn (C. Yuan), majiang@szu.edu.cn (J. Ma).

https://doi.org/10.1016/j.jmatprotec.2025.119178
Received 5 October 2025; Received in revised form 6 December 2025; Accepted 7 December 2025
Available online 8 December 2025

fundamental and unresolved reliance on thermal input. Liquid-state processes suffer from inhomogeneous reinforcement dispersion [9] and brittle intermetallic formation [14] due to high-temperature interfacial reactions, while deposition techniques face geometric constraints and low material utilization [15]. Even solid-state methods, despite avoiding melting, require elevated temperatures that induce powder oxidation [16] and residual porosity [17]. A fundamental limitation common to all these approaches is their pronounced dependence on high-temperature environments, which escalates equipment requirements and costs while exacerbating interfacial reactions and defect formation, ultimately degrading material performance. Notably, prior studies have focused on optimizing thermal parameters (e.g., temperature control [9,13], cooling rates [11]) rather than eliminating thermal input entirely—failing to address the root cause of performance degradation. This oversight raises a critical, unaddressed question: can robust, metallurgically bonded MMC interfaces be achieved through a purely athermal mechanism, thereby circumventing the inherent trade-offs between bonding strength and thermal-induced defects?

Metallic glasses (MGs), distinguished by their non-crystalline atomic structure circumventing lattice constraints, exhibit exceptional combinations of mechanical and functional attributes, including ultrahigh strength [18], superior elastic strain limit [19], excellent wear resistance [20], magnetic properties [21], catalytic and degradation properties [22], radiation tolerance [23], thermal cycling stability [24], and outstanding corrosion resistance [25]. Recent discoveries of liquid-like behavior in MG under ultrasonic vibration (UV)—achieved within milliseconds without thermal activation [26,27]—offer a promising athermal platform to manufacture composites with high-performance. Targeting the generic limitations of thermal processing in composite manufacturing, we propose a facile and flexible “cold manufacturing” strategy utilizing MG as a matrix to fabricate composites via UV. This work aims to validate the purely athermal nature of this mechanism—demonstrated by successful composite fabrication in extreme underwater and liquid nitrogen environments. The diffusion bonding mechanism is achieved through the synergistic coupling of mechanically activated flow and short-circuit diffusion paths. Building on this, disparate materials—ranging from conductors to insulators, metals to non-metals, and amorphous to crystalline systems—can be directly bonded to MGs via “cold manufacturing”, forming robust and intimate metallurgical interfaces. Futhermore, We also demonstrate that this approach establishes a versatile platform for precisely tailoring composite properties (e.g., Vickers hardness: 400–1450 HV; saturation magnetization: 0–158.6 emu/g). By doing so, it opens a generic pathway to composite design, free from the intrinsic limitations of heat.

2. Experimental

2.1. Raw material preparation

La-based ($La_{55}Al_{25}Ni_5Cu_{10}Co_5$), Zr-based ($Zr_{55}Cu_{30}Al_{10}Ni_5$ and $Zr_{35}Ti_{30}Be_{26.75}Cu_{8.25}$), Fe-based ($Fe_{78}Si_9B_{13}$) MGs, and TiZrHfBeNi high-entropy MGs were employed as core matrix materials. High-purity elemental constituents (>99.99 %) were arc-melted and cast into bulk specimens using water-cooled copper molds under low-pressure argon atmospheres. MG ribbons were fabricated via vacuum arc melting followed by melt-spinning onto a rapidly rotating copper wheel under high vacuum, or prepared through mechanical comminution. MG powders were synthesized utilizing vacuum arc melting coupled with high-pressure gas atomization.

2.2. Ultrasonic vibration joining process

The ultrasonic apparatus incorporates an ultrasonic generator producing electrical signals, a transducer converting these signals into mechanical vibrations, a booster amplifying vibration amplitude, and a sonotrode delivering high-frequency oscillations under controlled pressure. The UV joining mechanism necessitates contacting the joining materials with the sonotrode under approximately 200 N of preload force, followed by activation of high-frequency vibrations. The operational parameters comprised a vibration frequency of 20 kHz (± 500 Hz) with an amplitude of 44.4 μm (± 1 μm)—the maximum amplitude of the equipment, which ensures optimal bonding performance—with bonding performance at different amplitudes provided in the Supplementary Fig. 1. Process monitoring instrumentation included a custom-designed force sensor interfaced with a National Instruments NI-9237 data acquisition card operating at 1 kHz sampling frequency for pressure measurement. Concurrently, real-time temperature tracking employed a K-type thermocouple connected to a separate acquisition card (100 Hz sampling rate), achieving 0.2℃ measurement accuracy.

2.3. Mechanical and magnetic properties test

The hardness test was performed on MGs and composites using a Vickers hardness tester under a load of 500 gf (4.90 N) and held for 10 s. The hardness and modulus of the interface were measured by the Berkovich triangular pyramid indenter with a maximum load of 8 mN and constant loading rates of 5 mN/s, then held the load for 10 s. The magnetic hysteresis loops at room temperature were obtained by a magnetic measurement system (MPMS3) to test the magnetic properties of the composites.

2.4. Multi-scale structural characterizations

Structural characterization of all specimens was performed via X-ray diffraction (XRD, Rigaku MiniFlex 600) using Cu Kα radiation at 5° min^{-1} scan speed across the 20–80° 2θ range. Microstructural features and elemental distributions were examined using a field emission scanning electron microscope (SEM, FEI Quanta 450 FEG) with integrated energy-dispersive X-ray spectroscopy (EDS). Nanoscale morphological and structural assessments were conducted via transmission electron microscopy (TEM, Fei Titan Themis) with EDS capability, where specimens were prepared using an FEI Scios SEM/FIB dual-beam system. Three-dimensional analysis of joined MG interfaces employed X-ray computed tomography (CT, Sanying Precision Instruments nanoVoxel-3000d). Two complementary approaches were employed for Dynamic Scanning Probe Microscopy (DSPM) characterization: nano-dynamic mechanical analysis (nano-DMA) using a Hysitron TI950 nanoindenter (200 Hz tip frequency, 6 μN contact force) and amplitude modulation-frequency modulation (AM-FM) viscoelastic mapping via Oxford Instruments atomic force microscopy (72 kHz and 142 kHz operational frequencies). To ensure surface uniformity, all DSPM measurements utilized polished $Zr_{55}Cu_{30}Al_{10}Ni_5$ MG substrates.

3. Result and discussion

3.1. The process of cold manufacturing

It is generally accepted that the fabrication of metal matrix composites necessitates high temperatures, rendering cold manufacturing impossible. In this work, cold manufacturing of composites was achieved using UV technology in conjunction with MG materials. To substantiate the non-thermal nature of the manufacturing process, the MG matrix material and other additive phases were uniformly mixed. The raw materials, encompassing both ribbon and powder forms, were processed entirely underwater and in a liquid nitrogen environment, as schematically depicted in Fig. 1a. The aqueous environment, owing to its high specific heat capacity, effectively suppressed temperature rise—conditions under which conventional high-temperature processing would be incapable of successful composite fabrication. Meanwhile, the liquid nitrogen environment, with its boiling point of −196°C, is a recognized medium for creating extreme cryogenic conditions. Verification of the low-temperature and low-pressure characteristics of the

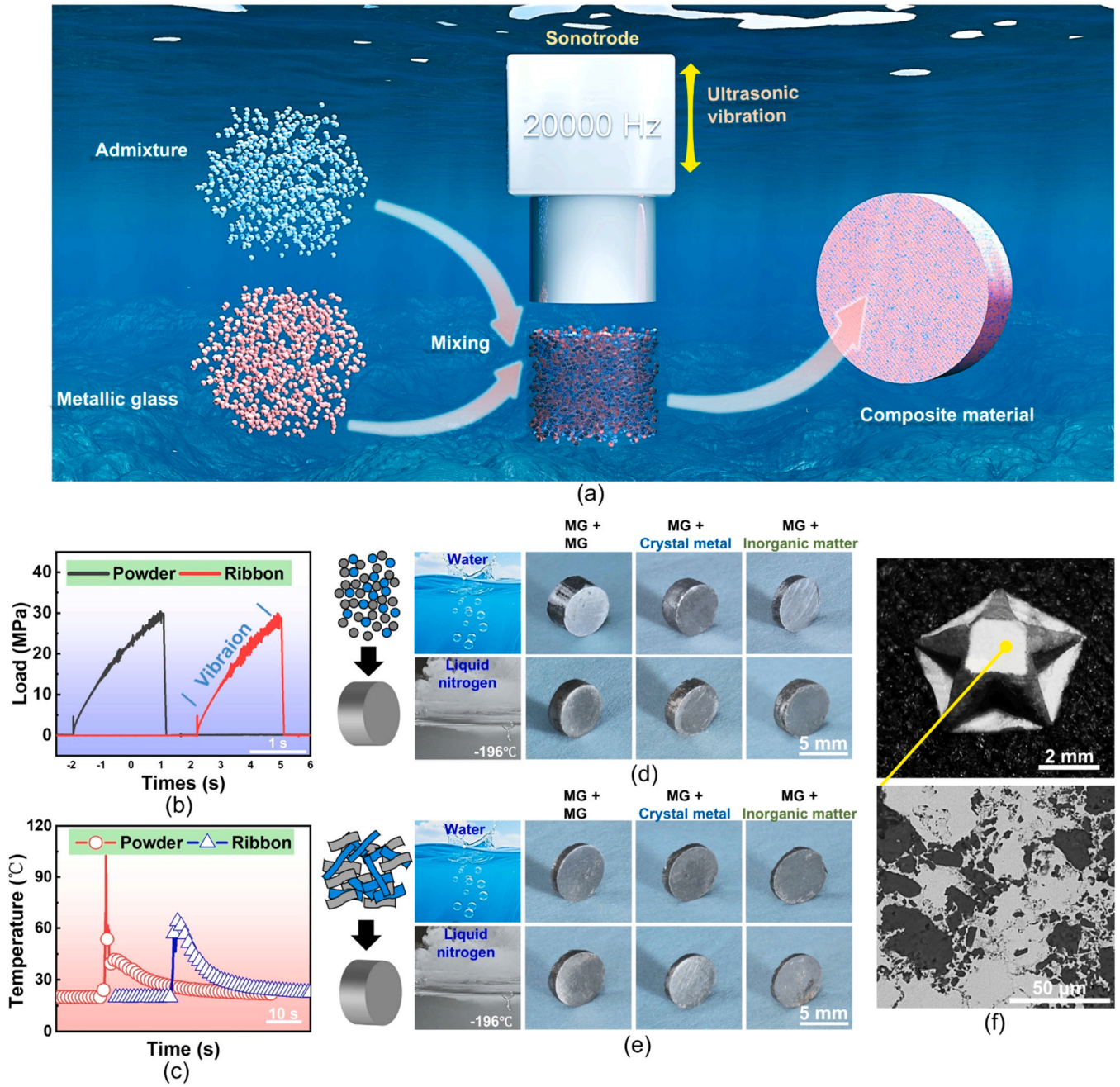

Fig. 1. The display of cold manufacturing process of metallic glass (MG)-based composite material. (a) The schematic diagram of composite manufacturing under cooling environment. (b) The stress-time curve of manufacturing process under water of MG-based composite material, including powder form and ribbon form. (c) The temperature-time curve of composite material manufacturing process under water, including powder form and ribbon form. (d, e) Samples display diagram of composite material fabricated by powder and ribbon raw materials ($Zr_{55}Cu_{30}Al_{10}Ni_5$ MG as matrix). (f) A three-dimensional pentagram-shaped composite material obtained by joining mixed powders ($Zr_{55}Cu_{30}Al_{10}Ni_5$ MG/Si_3N_4). The scanning electron microscope (SEM) images reveal that it exhibits a dense structure.

process was accomplished through in-situ, real-time monitoring of temperature and vibrational pressure during composite manufacturing. Taking the underwater environment as an example, the consolidation pressure for both powder- and ribbon-based composites, with comparable UV parameters employed, was registered at approximately 30 MPa (Fig. 1b)—significantly lower than pressures typical of conventional powder metallurgy techniques [28]. Magnified inspection of the pressure profile revealed high-frequency oscillations characteristic of the UV technique's action. The low temperatures recorded during underwater manufacturing further underscore the cold nature of the process. Using the $Zr_{55}Cu_{30}Al_{10}Ni_5$ MG / TiZrHfBeNi MG composite as an exemplar, which exhibited negligible thermal effects in water environments, with transient temperature spikes below 100°C persisting for merely 0.01–0.02 s. The maximum recorded temperatures for ribbon and powder specimens measured 90.1°C and 59.1°C, respectively (Fig. 1c), demonstrating values far below those required by conventional high-temperature manufacturing technologies.

Leveraging the unique room-temperature softening capability of metallic glasses, two distinct composite preparation routes were adopted: random stacking of ribbon fragments and uniform mixing of powders. Representative composites fabricated from powder raw materials (both underwater and in liquid nitrogen) are shown in Fig. 1d, while those made from ribbon raw materials (under the same two environments) are presented in Fig. 1e. These composites cover a remarkably

broad range of material combinations, including MG-MG, MG-crystalline alloy, and MG-nonmetallic (inorganic) composites. All manufactured composite samples exhibit regular geometries, retain a distinct metallic luster, and lack observable macro-defects, providing preliminary evidence of excellent bonding quality. Furthermore, UV-assisted joining enables synergistic control over the macroscopic geometry and internal phase distribution architecture of composite systems. As illustrated in Fig. 1f, a three-dimensional pentagram-shaped bulk component with a $Zr_{55}Cu_{30}Al_{10}Ni_5$ MG/Si_3N_4 composite structure was successfully fabricated. Macroscopic and microstructural examinations reveal that the as-prepared component achieves superior surface finish with well-defined edge definition.

3.2. Bonding quality characterization

Although various techniques exist for fabricating metal matrix composites, interfacial defects fundamentally limit their application potential. Consequently, interfacial bonding quality serves as a paramount indicator for evaluating composite reliability. A detailed characterization of the interfacial bonding quality in both ribbon-based and powder-based systems was conducted in this study, as presented in Figs. 2 and 3.

For the ribbon bonding system, the absence of significant void defects was revealed by computed tomography (CT) analysis in both cross-sectional and longitudinal sections of the $Zr_{55}Cu_{30}Al_{10}Ni_5$ MG / TiZrHfBeNi MG composite (Fig. 2a, b; the detail see Supplementary Fig. 2), indicating effective bonding across all regions. Analysis of the relative density distribution derived from the reconstructed CT data clearly delineated the internal two-phase structure of the material. Notably, the layered structure visible in the longitudinal slice image (Fig. 2b) originated from the stacked arrangement of the two distinct ribbons prior to bonding. Having confirmed the lack of macroscopic defects, further characterization was undertaken to assess the bonding quality at the microscopic scale. As shown in Fig. 2c, $Zr_{55}Cu_{30}Al_{10}Ni_5$ MG ribbons themselves achieve seamless, intimate contact without inducing crystallization, demonstrating their inherent favorable bonding characteristics. Subsequently, composites were fabricated by stacking $Zr_{55}Cu_{30}Al_{10}Ni_5$ MG ribbons (acting as the matrix) with La-based ($La_{55}Al_{25}Ni_5Cu_{10}Co_5$, Fig. 2d), high-entropy (TiZrHfBeNi, Fig. 2e), and Fe-based ($Fe_{78}Si_9B_{13}$, Fig. 2f) MG ribbons. The results demonstrate that each type of MG can form a void-free, metallurgically bonded interface with the Zr-based MG via the stacking and bonding approach, with no observable crystallization (Fig. 2c-f).

The feasibility of achieving MG-MG bonding is theoretically underpinned by the ability of UV to induce plastic deformation in metallic glasses. However, the more challenging question concerns the ability to bond MG with non-MG materials, which dictates the universality of MG-based composite technology since most engineering materials are crystalline. To address this, composites were initially fabricated by stacking MG ribbons with crystalline metals, such as Al alloys and CoCrFeNiMn high-entropy alloy. X-ray diffraction (XRD) analysis confirmed the absence of crystallization, showing distinct peaks for the crystalline phases while no crystalline signatures were detected near the broad amorphous hump (Fig. 2g). The cross-section of the Zr-based MG / CoCrFeNiMn high-entropy alloy composite revealed a well-defined alternating layered structure. In contrast, the Zr-based MG / Al composite displayed a more intermixed structure (Fig. 2h), possibly related to the facile deformation of Al under ultrasonic vibration. High-magnification scanning electron microscopy (SEM) and energy-dispersive X-ray spectroscopy (EDS) analysis at the interfaces confirmed the formation of defect-free metallurgical bonds between the MG and crystalline materials (Fig. 2h). Furthermore, ribbon-based composites incorporating non-metallic materials (glass fiber, carbon fiber) were explored. Their diffraction patterns exhibited characteristic amorphous features typical of both the metallic glass and the non-metallic phase (Fig. 2i). SEM imaging of cross-sections showed that the fiber particles were distributed as band-like enrichments within the MG matrix (Fig. 2j), achieving seamless bonding at the MG/fiber interface.

For the powder bonding system, achieving complete metallurgical bonding is widely acknowledged to be challenging due to the numerous interfaces and the inherent presence of surface oxide layers [27,29]. Nevertheless, CT scans of the $Zr_{55}Cu_{30}Al_{10}Ni_5$ MG / TiZrHfBeNi MG powder composite fabricated via the UV process revealed no macro-defects and a uniform distribution of both phases (Fig. 3a, b; the detail see Supplementary Fig. 3). UV consolidation of $Zr_{55}Cu_{30}Al_{10}Ni_5$ MG powder mixed with La-based (Fig. 3d), high-entropy amorphous (Fig. 3e), and Fe-based (Fig. 3f) MG powders consistently yielded fully amorphous composite bulk materials. However, the bonding mode differed significantly from the ribbon system. The Zr_{55}-La_{55} combination formed a core-shell structure, where the La-based MG coats the Zr-based particles (Fig. 3d). The Zr-TiZrHfBeNi system exhibited concurrent softening of both components prior to interfacial merging (Fig. 3e). In contrast, the Zr-based/Fe-based system featured a Zr-based MG matrix embedding the Fe-based MG particles (Fig. 3f), a result of the preferential softening of the Zr-based MG. These variations stem from the distinct ultrasonic softening kinetics intrinsic to the different materials: the La-based MG exhibits accelerated viscoelastic transition, the Zr-based and TiZrHfBeNi MG show similar softening behaviors, and the Fe-based MG is the most resistant to softening. Utilizing fine powder particles, the UV process not only achieved strong bonding between MGs but also successfully enabled robust bonding between MG and crystalline metals (e.g., CoCrFeNiMn high-entropy alloy, 1060Al) and non-metallic materials (e.g., SiO_2, Si_3N_4), preserving the amorphous character of the MG matrix (Fig. 3g–j). With the exception of the MG-Al composite (Fig. 3h), all other systems displayed the non-MG particles embedded within the MG matrix, exhibiting continuous bonding at the interface.

3.3. The mechanisms of cold manufacturing

A process for fabricating composites at low temperatures has been successfully realized, exhibiting no excessive temperature rise as demonstrated in Fig. 1d. This finding implies the existence of a unique bonding mechanism independent of temperature elevation, enabling perfect manufacturing under any thermal condition. Previous characterizations (Figs. 1, 2, 3) collectively demonstrate that all bonding phenomena originate from the softening flow of the MG.

This phenomenon is defined as Ultrasonic vibration-induced plasticity (UVIP) —a concept consistent with the MG softening we observed [26]. MGs exhibit structural heterogeneity due to the coexistence of liquid-like zones (LLZs) and solid-like zones (SLZs) [30]. The SLZs form a continuous network skeleton responsible for elastic deformation, while the embedded LLZs act as viscoelastic flow units that dissipate energy during deformation [31]. Under localized shear loading, LLZs absorb significant energy and undergo dilation, promoting their growth and coalescence [32]; this evolution is key to plastic flow initiation here. Critically, the UVIP process involves high-frequency vibrational loading (up to 20 kHz). Drawing parallels with high-frequency cyclic loading studies on structurally heterogeneous saturated soil models, the insufficient stress relaxation time within LLZs leads to persistent accumulation of transient high pressure [33], insufficient LLZ stress relaxation (under UV) causes transient high pressure—analogous to the soil mechanism. Upon UV application, LLZs rapidly dilate and penetrate the SLZ network. Once interconnected LLZs form dominant percolation channels, the elastic network skeleton undergoes deconstruction, triggering bulk viscous softening behavior [26].

To experimentally elucidate the UVIP mechanism, the viscoelastic loss tangent ($\tan\delta$) of Zr-based MGs was characterized using a Dynamic Scanning Probe Microscopy (DSPM) system (Fig. 4a-c). Here, δ represents the phase shift between dynamic force and displacement amplitude (experimental details in Methods). The results show excellent

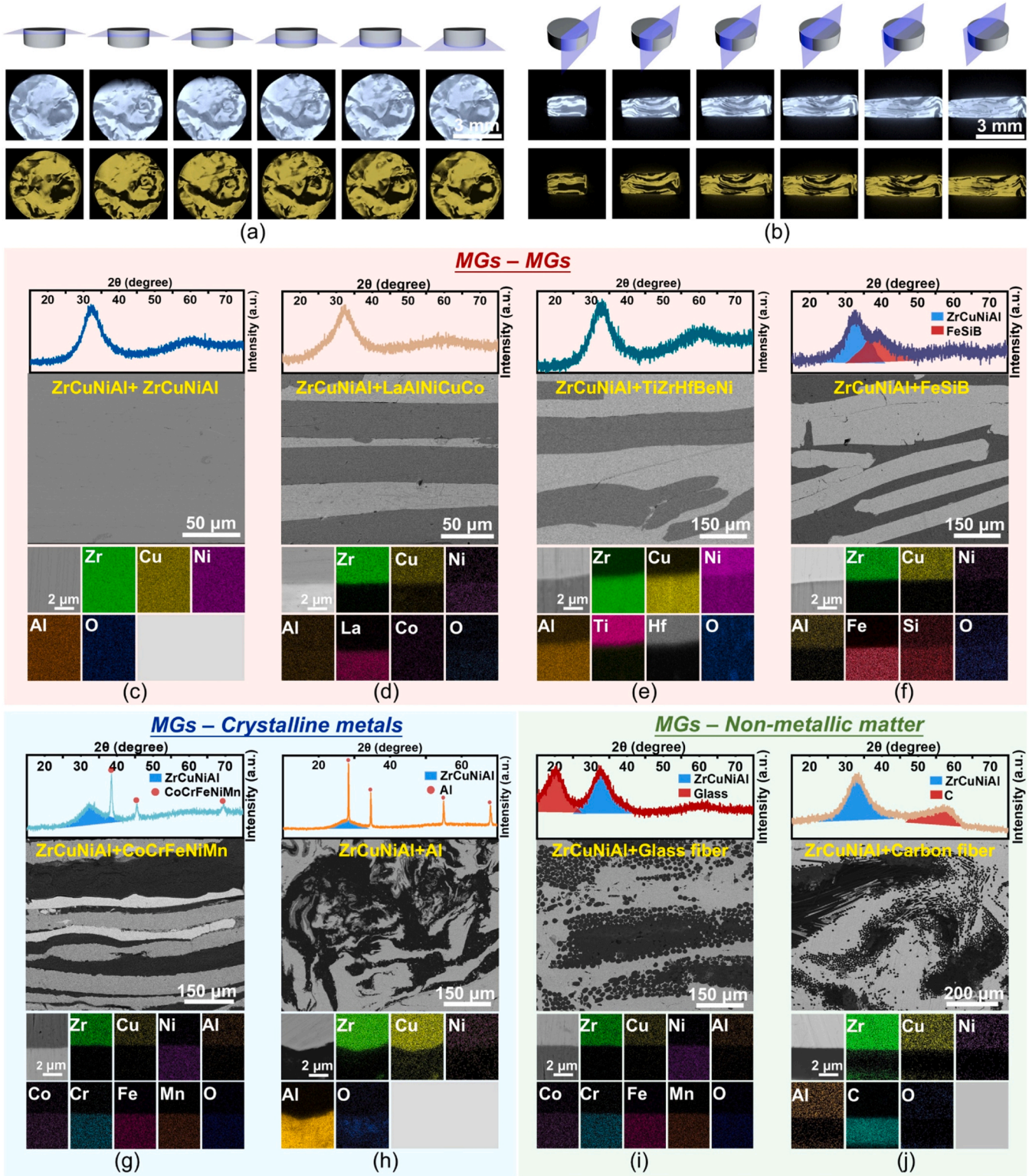

Fig. 2. Ribbon matrix composites. (a, b) Computed tomography (CT) scans and density profiles of $Zr_{55}Cu_{30}Al_{10}Ni_5$ MG/TiZrHfBeNi metallic glass (MG) composites, showing longitudinal and cross-sectional views. (c) X-ray diffraction (XRD) patterns and field-emission scanning electron microscope (SEM) micrographs of pure $Zr_{55}Cu_{30}Al_{10}Ni_5$ MG bonded samples. And the $Zr_{55}Cu_{30}Al_{10}Ni_5$ MG bonding interface with corresponding energy-dispersive X-ray spectroscopy (EDS) elemental mapping. (d) XRD, SEM, and EDS analyses of $Zr_{55}Cu_{30}Al_{10}Ni_5$ MG/$La_{55}Al_{25}Ni_5Cu_{10}Co_5$ MG composites. (e) XRD, SEM, and EDS analyses for $Zr_{55}Cu_{30}Al_{10}Ni_5$ MG/ TiZrHfBeNi MG composites. (f) XRD, SEM, and EDS analyses of $Zr_{55}Cu_{30}Al_{10}Ni_5$ MG/ $Fe_{78}Si_9B_{13}$ MG composites. (g) XRD, SEM, and EDS characterization of $Zr_{55}Cu_{30}Al_{10}Ni_5$ MG/CoCrFeNiMn composites. (h) XRD, SEM, and EDS analyses for $Zr_{55}Cu_{30}Al_{10}Ni_5$ MG/Al alloy (1060 Al) composites. (i) XRD, SEM, and EDS analyses of $Zr_{55}Cu_{30}Al_{10}Ni_5$ MG/glass fiber composites. (j) XRD, SEM, and EDS analyses of $Zr_{55}Cu_{30}Al_{10}Ni_5$ MG/carbon fiber composites.

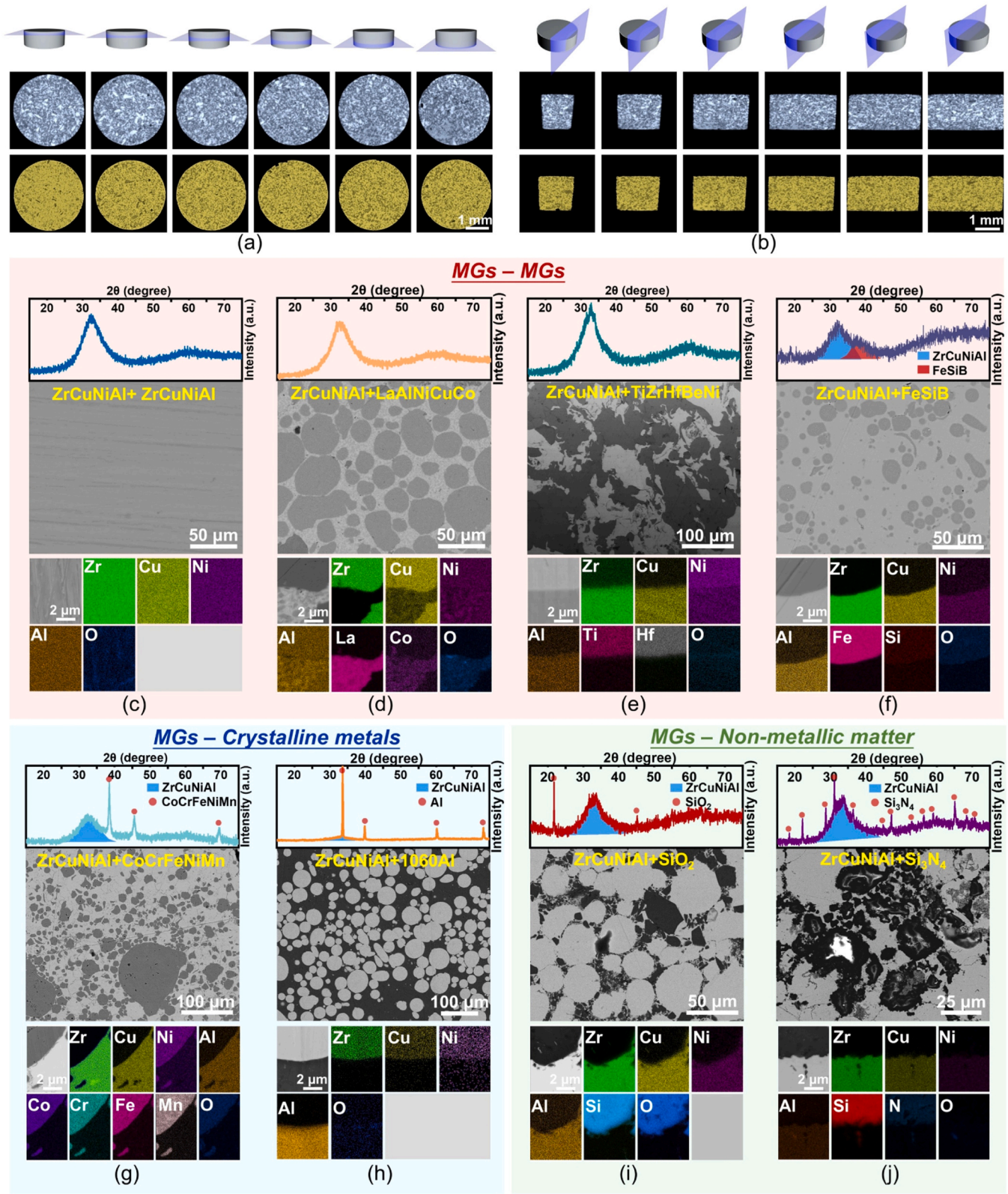

Fig. 3. Powder matrix composites. (a, b) Computed tomography (CT) scans and density profiles of $Zr_{55}Cu_{30}Al_{10}Ni_5$ MG/TiZrHfBeNi metallic glass (MG) powder-boned composites, showing longitudinal and cross-sectional views. (c) X-ray diffraction (XRD) patterns and field-emission scanning electron microscope (SEM) micrographs of pure $Zr_{55}Cu_{30}Al_{10}Ni_5$ MG powder-boned samples. And the $Zr_{55}Cu_{30}Al_{10}Ni_5$ MG bonding interface with corresponding energy-dispersive X-ray spectroscopy (EDS) elemental mapping. (d) XRD, SEM, and EDS analyses of $Zr_{55}Cu_{30}Al_{10}Ni_5$ MG/$La_{55}Al_{25}Ni_5Cu_{10}Co_5$ MG composites. (e) XRD, SEM, and EDS analyses for $Zr_{55}Cu_{30}Al_{10}Ni_5$ MG/TiZrHfBeNi MG composites. (f) XRD, SEM, and EDS analyses of $Zr_{55}Cu_{30}Al_{10}Ni_5$ MG/ $Fe_{78}Si_9B_{13}$ MG composites. (g) XRD, SEM, and EDS characterization of $Zr_{55}Cu_{30}Al_{10}Ni_5$ MG/CoCrFeNiMn composites. (h) XRD, SEM, and EDS analyses for $Zr_{55}Cu_{30}Al_{10}Ni_5$ MG/Al alloy (1060 Al) composites. (i) XRD, SEM, and EDS analyses of $Zr_{55}Cu_{30}Al_{10}Ni_5$ MG/SiO_2 composites. (j) XRD, SEM, and EDS analyses of $Zr_{55}Cu_{30}Al_{10}Ni_5$ MG/Si_3N_4 composites.

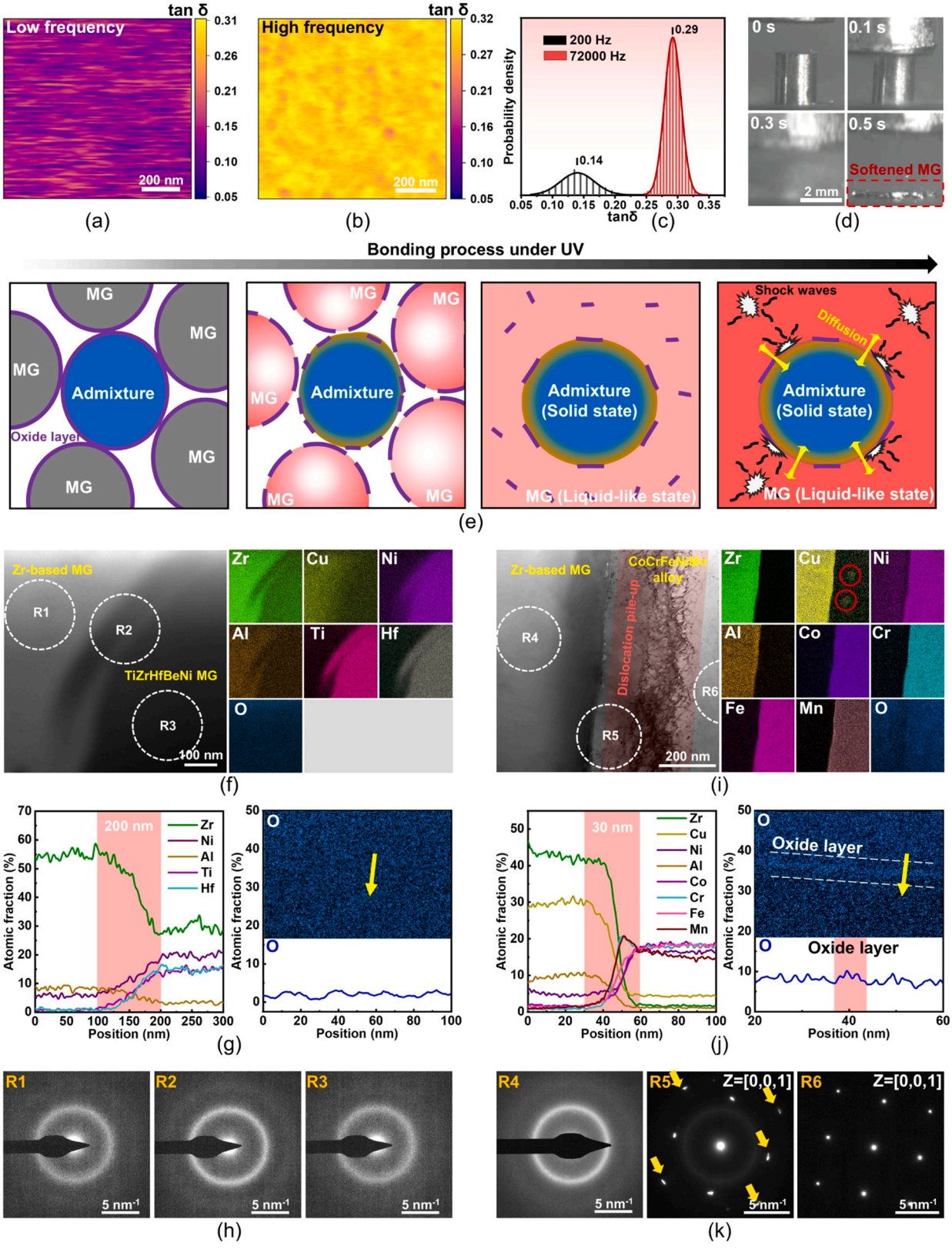

Fig. 4. Joining mechanisms. (a-b) The viscoelastic loss tangent map at $f = 200$, 72000 Hz. (c) The statistical analysis of a and b with a good fit of Gaussian distribution. (d) Softening process of $Zr_{55}Cu_{30}Al_{10}Ni_5$ metallic glass (MG) captured by high-speed camera. (e) Schematic diagram illustrating the joining mechanism between metallic glass and other materials, showing the softening and atomic activity activation of the MG and the surface activation of the addtive material. (f) High-angle annular dark-field (HAADF) image of the interface in the MG-MG composite ($Zr_{55}Cu_{30}Al_{10}Ni_5$ MG / TiZrHfBeNi MG) sample and corresponding energy-dispersive X-ray spectroscopy (EDS) elemental maps. (g) EDS linescan of interface and oxide layer. (h) High-resolution TEM image and selected-area electron diffraction (SAED) patterns corresponding to regions R1, R2, and R3 in f. (i-k) HAADF, EDS mapping, EDS linescan of interface and oxide layer, and SAED images of the interface in the MG-high-entropy alloy composite ($Zr_{55}Cu_{30}Al_{10}Ni_5$ MG / CoCrFeNiMn high-entropy alloy) sample.

agreement with conventional dynamic mechanical analysis (DMA) data, validating the methodology. Based on tanδ mapping of Zr-based MG at probe frequencies of 200 Hz and 72,000 Hz, two distinct response modes were identified. Statistical analysis revealed pronounced dynamic heterogeneity at 200 Hz, with tanδ exhibiting an ideal Gaussian distribution. At 72,000 Hz, the mean tanδ increased to 0.29 (Fig. 4(a-c)), while dynamic heterogeneity remained observable. To quantify the high-frequency loading effect on MG softening, viscosity evolution was derived from tanδ [34]. Utilizing a simplified Maxwell model [35], the relationship $\tau = 1/(\omega \cdot \tan\delta)$ [35,36] was employed (where τ is relaxation time and ω is angular frequency). Experimentally, τ is proportional to viscosity in such viscoelastic systems. Comparative viscosity (or τ) data across frequencies were yielded via model simplification. The calculations indicated that viscosity (or τ) decreased by three orders of magnitude when frequency increased from 200 Hz to 72,000 Hz. Concurrently, experiments confirmed rapid softening of $Zr_{55}Cu_{30}Al_{10}Ni_5$ MG monoliths under UV within a temperature-limited enclosed underwater environment (Fig. 4d; Supplementary Video 1), providing direct evidence for this unique mechanism. In contrast, crystallized MGs exhibited brittle fracture rather than softening under identical conditions [37].

Building upon the concept of ultrasound-induced MG softening, the mechanism for fabricating MG-based composites, using powder composites as a prototype, is proposed (Fig. 4e). Initially, during early-stage UV treatment, both MG and additive powders are solid. Their mutual friction under high-frequency vibration partially removes surface oxide layers. The MG, being highly sensitive to the UV field, is first affected, activating its internal amorphous structure. Subsequently, the softening flow effect emerges in the MG. At this stage, UV activates two phenomena common in classical viscoelastic fluids—acoustic streaming and cavitation [38], primarily caused by energy attenuation during wave propagation. These nonlinear effects induce directional flow in the liquid-like material, generating intense localized shockwaves and strong convective mass transfer within the fluid, with particularly significant impact at solid-liquid interfaces [39,40]. During this process, oxide layers on the MG surface are fragmented by microjets and shocks from cavitation, eliminating barriers to flow. Simultaneously, the softened/collapsed MG melt is instantly exposed, enabling full contact and mixing with additive powder particles not yet activated by vibrational softening, thereby filling interfacial gaps. Continued ultrasonic treatment not only progressively reduces the viscosity of the fluidized MG but also significantly enhances atomic mobility (atomic activity, $\mu \propto 1/\tau$; note τ decreased by three orders of magnitude) [41,42]. Crucially, shockwaves and convective mass transfer effects are highly concentrated at interfaces between fluid-like MG and solid additive particles. Under thermal heating conditions, MGs within the supercooled liquid region have been demonstrated to form metallurgical bonding at solid-liquid interfaces [43], with their tanδ values comparable to those observed in the present work [44]. More importantly, the shock waves and mass transfer effects concentrated at the interface between the fluid-like MG and the solid additives provide the key driving force for atomic interdiffusion. This diffusion process is essentially a synergistic coupling of mechanical and thermodynamic forces: ultrasonically induced acoustic streaming and cavitation mechanically transport MG atoms to the additive surface via convective mass transfer and micro-jets, achieving intimate atomic-scale contact. Simultaneously, the localized shock waves and non-equilibrium conditions generated by cavitation collapse significantly activate the interfacial region [39,40]. On the thermodynamic side, the markedly enhanced atomic mobility in the softened MG enables rapid atomic movement, while the inherent chemical potential gradient at the newly formed interface provides a sustained driving force for mutual diffusion. Furthermore, the ultrasound-induced vacancy concentration gradients and stress fields create short-circuit diffusion paths, further accelerating atomic migration [45]. Therefore, the final interfacial metallurgical bonding is achieved through the synergistic interaction of mechanical activation, chemical potential gradients, and enhanced diffusion kinetics.

To obtain definitive evidence for the bonding mechanism, we characterized the interfaces in two types of composites: (1) an MG-MG interface (specifically, $Zr_{55}Cu_{30}Al_{10}Ni_5$ MG / TiZrHfBeNi MG), and (2) an MG-non-MG interface (represented by a Zr-based MG / CoCrFeNiMn high-entropy alloy interface). Consistent with the proposed composite bonding mechanism, substantial differences were expected and observed between these two bonding configurations. Analysis of the MG-MG interface reveals a tortuous morphology (Fig. 4f), suggestive of mutual liquid-phase stirring. Line-scanning analysis across the interface (Fig. 4g) indicates an interfacial mutual diffusion zone $\approx$ 100 nm thick. Crucially, the oxygen signal remains stable across this zone, demonstrating complete elimination of the native oxide layer. This phenomenon arises because both MGs simultaneously soften into a fluidic state under ultrasonic vibration. Continued ultrasonic agitation fragments the oxide layer, and the fragmented oxide nanoparticles disperse within the flowing matrix material. Remarkably, despite achieving perfect atomic-scale metallic bonding (see Supplementary Fig. 4), both sides of the interface and the interfacial region itself retain a fully amorphous structure (Fig. 4h). Collectively, these multiscale characterizations demonstrate that the internal structure of the composite forms an integral metallurgical bond, rather than a mere mechanical interlock.

Conversely, while the MG-CoCrFeNiMn interface (Fig. 4i) also can not see voids or gaps at the nanoscale, its morphology differs significantly: it is straight. This distinct form arises because the crystalline CoCrFeNiMn alloy cannot undergo the characteristic softening and flow behavior inherent to amorphous structures; during welding, only the MG phase softens. Notably, an exceptionally high density of dislocations was observed at the interface, concentrated on the CoCrFeNiMn side (Fig. 4i). In contrast to the surface region, the dislocation density within the bulk of the particles is significantly lower (see Supplementary Fig. 5). The dislocation generation is directly caused by the sever deformation under the high-frequency cyclic stress field of ultrasonic oscillation. Although the stress amplitude is below the macroscopic yield strength of the additive particles, the 20,000 Hz cyclic loading (50 μs per cycle) reduces the activation barrier for dislocation motion through a periodic stress field and is sufficient to activate dislocation sources at local defects [46]. This process can simultaneously activate multiple slip systems, leading to substantial dislocation multiplication [47]. Notably, regions of intense defect accumulation at the interface exhibit localized partial amorphization, contrasting sharply with the crystalline interior structure (see Supplementary Fig. 6). The resulting high dislocation density and other defect at the surface significantly enhances the vacancy concentration gradient and the stress gradient as the strong diffusion path [45]. Upon contact with the ultrasonically liquefied MG—possessing inherently higher atomic mobility—mutual diffusion occurs. EDS mapping detected Cu-enriched zones within the CoCrFeNiMn side near the interface (Fig. 4i), corroborating this diffusion process. Line-scanning analysis (Fig. 4j) revealed a total interdiffusion zone depth of $\approx$ 20–30 nm at this interface. While shallower than that observed in the MG-MG case, this diffusion depth remains sufficient for robust bonding. Surprisingly, oxygen analysis revealed the presence of a thin ($\approx$5 nm) oxygen-enriched layer at the interface, yet its oxygen concentration was substantially lower than the characteristic value of the native oxide (Fig. 4j). As oxide layers are widely recognized as significant barriers to material bonding, this finding demonstrates two critical advantages: (1) diffusion can surpass the oxide barrier between the MG and its counterpart; and (2) the bonding process concomitantly weakens the oxide layer (reducing its oxygen content), thereby mitigating potential performance degradation at the interface. These capabilities possess considerable research significance. Selected-area electron diffraction (SAED) analysis provided further interfacial insights (Fig. 4k). Sharp amorphous halos were obtained from the MG side and distinct crystalline diffraction spots from the CoCrFeNiMn side. The interfacial region itself exhibited diffraction features indicative of co-existing crystalline and amorphous phases. The crystalline diffraction

spots observed within the interfacial zone provide evidence for significant interfacial lattice distortions, correlating with the high dislocation density observed in the corresponding HAADF-STEM image (R5 in Fig. 4k).

3.4. Performance regulation

The pursuit of designing materials with ideal and customizable properties has remained a fundamental objective and continues to drive significant research interest in materials science. These unique characteristics of MGs enable effective joining with diverse material categories spanning conductors to insulators, and metallic to non-metallic systems, as demonstrated in Figs. 2 and 3. This compatibility facilitates the in situ fabrication under special conditions through UV joining techniques. The resulting composites can be engineered to achieve tailored multifunctional characteristics that address specific application requirements.

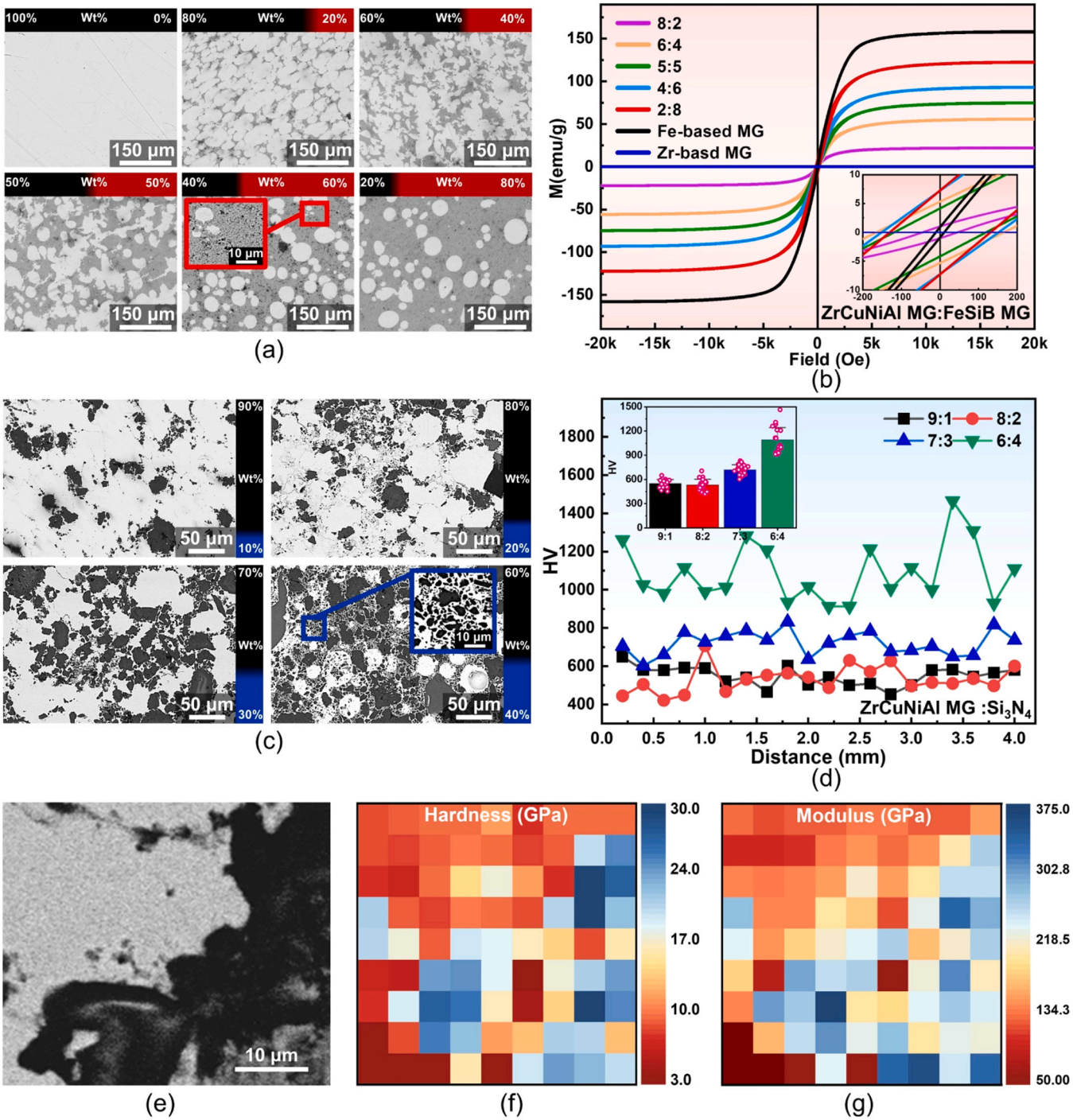

Fig. 5. Performance tuning. (a) The internal high-resolution scanning electron microscope (SEM) images of Zr-based MGmetallic glass (MG) combined with Fe-based MG in the weight ratios of 8:2, 6:4, 5:5, 4:6, and 2:8 (wt%) at low magnification. (b) The magnetic property tuning of the composites formed by $Zr_{55}Cu_{30}Al_{10}Ni_5$ MG and $Fe_{78}Si_9B_{13}$ MG powders at different ratios. (c) Internal SEM images of Zr-based MG combined with Si_3N_4 in the weight ratios of 9:1, 8:2, 7:3, and 6:4 (wt%) at low magnification. (d) The mechanical property tuning (microhardness test) of the composites formed by $Zr_{55}Cu_{30}Al_{10}Ni_5$ MG and Si_3N_4 powders at different ratios. The inset show columnar comparison chart, Error bars represent ± SD from the mean value (n = 20) (e-g) The hardness and modulus distribution map detected by nanoindentation in the interface of the $Zr_{55}Cu_{30}Al_{10}Ni_5$ MG/Si_3N_4 composite.

Using the underwater environment as a case study, we demonstrate magnetic property modulation through the strategic integration of Zr-based MGs possessing exceptional ultrasonic softening characteristics with Fe-based MGs exhibiting superior soft magnetic behavior. Fig. 5a presents cross-sectional SEM images of the composite materials, accompanied by mass ratio indicators for compositional differentiation. Microstructural analysis reveals significant phase content variations across different mixing ratios. Notably, composites with Zr-dominated compositions (8:2, 6:4, 5:5) exhibit defect-free consolidation with dense interfacial bonding, and Fe-dominated systems (4:6, 2:8) exist in localized void structures (Fig. 5a). Fig. 5b displays room-temperature hysteresis loops quantifying the magnetic response evolution. A remarkable magnetic contrast emerges between parent materials: Fe-based MG achieves superior saturation magnetization (Ms=158.6 emu/g), while Zr-based MG shows negligible magnetic response (Ms=0 emu/g). The composite magnetization demonstrates precise compositional tunability, with M_s values progressing systematically from 22.6 emu/g to 122.1 emu/g (corresponding to Fe-based MG contents of 20–80 wt%). This progression follows the sequence: 22.6→55.9→74.4→93.6→122.1 emu/g, establishing a nearly linear dependence on ferromagnetic phase concentration. The coercivity of the composites is slightly higher than that of the pristine samples (Fig. 5b).

Additionally, the investigation systematically examines mechanical property regulation in composites fabricated, focusing on $Zr_{55}Cu_{30}Al_{10}Ni_5$ MG integration with rigid Si_3N_4. Experimental results confirm effective interfacial bonding between the Zr-based MG and Si_3N_4 (Fig. 5c). Notably, Si_3N_4-dominated systems (6:4 ratio) exhibit crushed particle comminution to nanoscale dimensions, enabling effective nanoparticle incorporation within the ultrasonically softened matrix and enhanced diffusion bonding. Mechanical characterization through hardness testing reveals composition-dependent performance evolution (Fig. 5d). At lower Si_3N_4 contents (10–20 wt%, 9:1–8:2 ratios), hardness values (400–700 HV) showed small improvement relative to as-cast $Zr_{55}Cu_{30}Al_{10}Ni_5$ MG (517 HV). A critical threshold emerges at 30 wt% Si_3N_4 (7:3 ratio), with hardness escalating to 600–830 HV. Maximum performance is achieved at 40 wt% reinforcement (6:4 ratio), where hardness surges to 900–1450 HV, a 2.8-fold enhancement over the base MG. This remarkable amplification correlates with both increased Si_3N_4 content and optimized distribution of ultrafine fragmented particulates.

To verify the densification of materials with different doping ratios, relative density analysis was conducted. The density experiments employed Archimedes' method to compare the actual density with the theoretical density for MG, Si_3N_4, and the composites. The actual density of the composites should be calculated using the following formula:$\rho_{actual} = (\omega_1 \times \rho_{water})/(\omega_1 - \omega_2)$. where ρ_{water} denotes the density of distilled water, assumed to be 0.999 g cm^{-3} at room temperature, and ω_1 and ω_2 represent the weight of the sample in air and in distilled water, respectively. The theoretical density of the composites (ρ_{calc}) should be calculated using the following formula:

$$\rho_{calc} = \frac{(\omega_{MG} + \omega_{admixture})}{(\omega_{MG}/\rho_{MG} + \omega_{admixture}/\rho_{admixture})} \quad (1)$$

In Eq. (1) ω_{MG} represents the weight of Zr-based MG, $\omega_{admixture}$ is the weight of admixture, ρ_{MG} represents the density of Zr-based MG, and $\rho_{admixture}$ represents the densities of the admixture. After calculation, the theoretical density ρ_{calc} of the composites is 6.123, 5.556, 5.081, and 4.684 g cm^{-3} . The maximum error between the actual density and the theoretical density is only 2 %, indicating that the bonding is very intact and solid (see Supplementary Fig. 7).

To assess interfacial reliability in composite systems, nano-indentation mapping was employed to characterize mechanical property gradients across $Zr_{55}Cu_{30}Al_{10}Ni_5$ MG/Si_3N_4 interfaces (Fig. 5e). The spatial profiles reveal distinct hardness and modulus disparities between constituent phases (Fig. 5f, g), with no detectable mechanical degradation at interfacial regions. These findings collectively validate the dual capability of UV joing technology: achieving precise performance modulation while maintaining exceptional interfacial structural integrity in dissimilar material systems.

3.5. Structural design of composites

An innovative strategy for structure-property regulation of composites was developed through precisely engineered material composition and architectural design, as illustrated in Fig. 6a. Initially, $Zr_{55}Cu_{30}Al_{10}Ni_5$ and $Zr_{35}Ti_{30}Be_{26.75}Cu_{8.25}$ metallic glass (MG) powders were alternately stacked. This underwater processing technique successfully fabricated a densified laminated biphasic MG bulk composite, with cross-sectional morphology and corresponding elemental mapping confirming its highly compacted architecture (Fig. 6b).

Furthermore, beyond the MG laminate system, crystalline 6061Al alloy powder was incorporated into this process. Results demonstrate that this structural design extends beyond MG-MG bonding, simultaneously achieving high-quality metallurgical interfacial bonding between MG-Al alloy and Al alloy-Al alloy interfaces (Fig. 6c). The technique exhibits exceptional compatibility with multi-material systems—exemplified by the successful fabrication of laminated structures using three distinct powder components—thereby establishing a novel pathway for designing multi-component hierarchical composites with tailorable properties.

4. Conclusion

This study establishes a "cold manufacturing" paradigm utilizing MGs, which fundamentally resolves the longstanding compromise in composite fabrication between achieving robust metallurgical bonding and preventing thermal degradation. By exploiting an ultrasonically activated athermal plasticity mechanism, we demonstrate a general principle for solid-state diffusion bonding at low temperature. The successful fabrication of composites in extreme underwater and cryogenic environments provides definitive validation of this purely athermal process. Consequently, this work delivers a versatile manufacturing platform that decouples precise property tuning from thermal processing constraints. The key conclusions are as follows:

(1) The core of this paradigm involves using the ultrasonically activated athermal plasticity of metallic glasses, coupled with surface activation of the additive material, to achieve room-temperature metallurgical bonding. This process induces transient softening and high atomic mobility within the metallic glass matrix. This activated state allows the matrix to interact with the UV induced defect-rich surface of the additive material. Consequently, seamless interfaces with diverse materials, including conductors, insulators, metals, and non-metals, are formed via solid-state diffusion, bypassing the need for thermal activation.

(2) This mechanism establishes a general and distinct principle for composite fabrication and solid-state joining. It replaces thermal activation with controlled mechanical (ultrasonic) activation, thereby presenting a universal strategy applicable to a broad range of heat-sensitive or thermally incompatible material systems. This principle directly overcomes the intrinsic bottlenecks of conventional metal-matrix composite processing, such as interfacial reactions, reinforcement degradation, and porosity induced by high temperatures.

(3) The approach constitutes a highly tunable manufacturing platform. By adjusting the metallic glass binder ratio and the composition of the added phases, the mechanical and functional properties of the resulting composites can be precisely engineered, as demonstrated by the tailored Vickers hardness (400–1450 HV) and saturation magnetization (0–158.6 emu/g). This demonstrates that property programming and strong

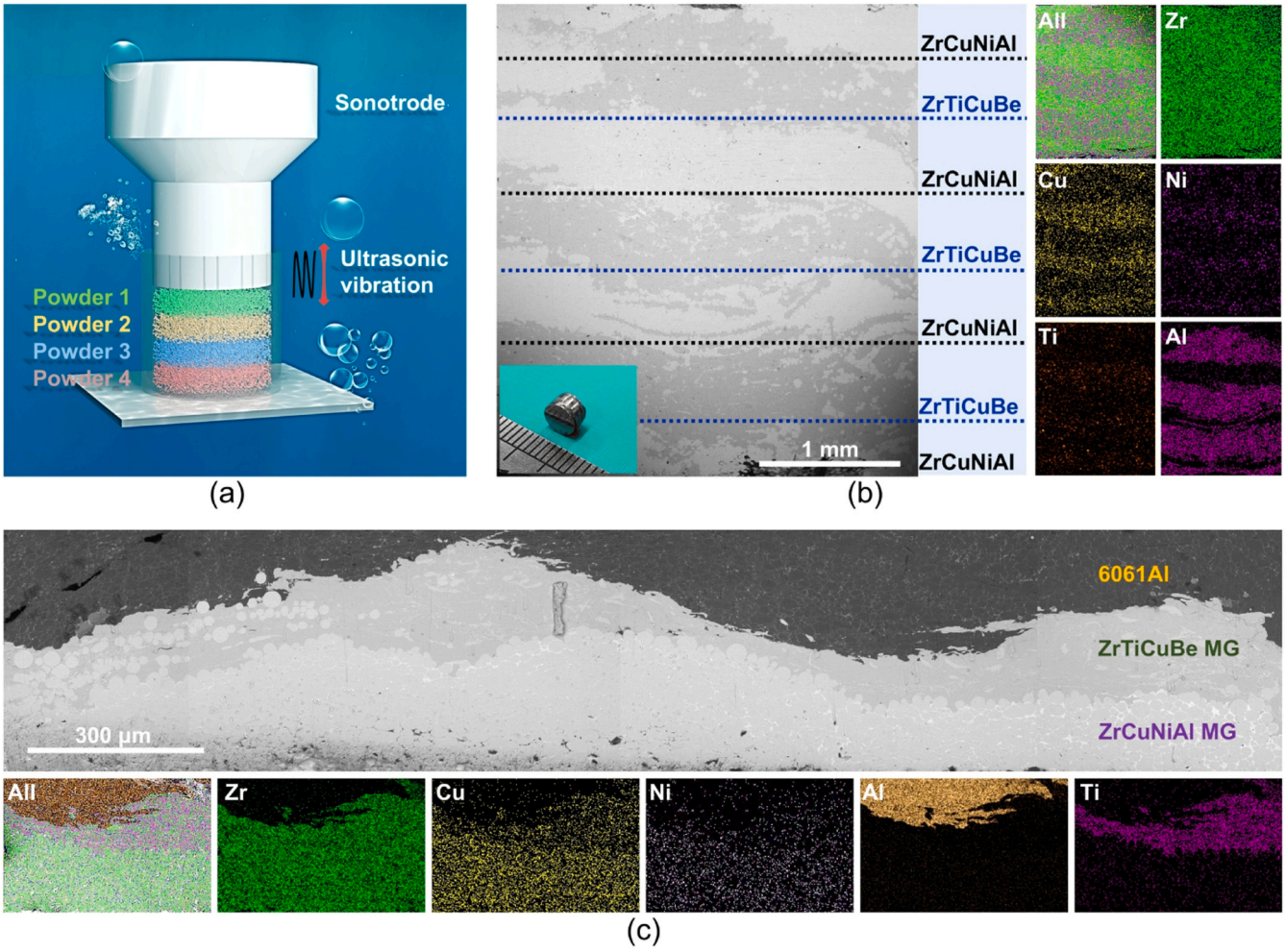

Fig. 6. Additive manufacturing of dissimilar materials in extreme environments by using ultrasonic vibration. (a) Schematic diagram of additive manufacturing in extreme environments by ultrasonic vibration. (b) Formation of $Zr_{55}Cu_{30}Al_{10}Ni_5/Zr_{35}Ti_{30}Be_{26.75}Cu_{8.25}$ layered structures via powder joining under water. (c) Formation of Al alloy/$Zr_{35}Ti_{30}Be_{26.75}Cu_{8.25}$ MG/$Zr_{55}Cu_{30}Al_{10}Ni_5$ MG layered structures via powder joining under water.

interfacial bonding can be simultaneously achieved, completely decoupled from thermal processing pathways.

(4) The purely athermal nature of the process grants it unique compatibility with extreme environments, as conclusively proven by successful fabrication underwater and in liquid nitrogen. This capability enables the in-situ synthesis and consolidation of composites in previously inaccessible scenarios, such as in space, deep-sea, or cryogenic settings, and is particularly vital for integrating components with vastly different thermal expansion coefficients or stability profiles.

Building upon the validated mechanism and platform capabilities, future research will focus on expanding the library of additive materials and diversifying the spectrum of property tuning—encompassing mechanical, catalytic, electrical, and magnetic properties. Efforts will also be dedicated to developing quantitative process-structure-property models to enable predictive manufacturing. These initiatives are expected to pave the way for novel composite materials with outstanding comprehensive performance.

CRediT authorship contribution statement

Zhe Chen: Validation, Data curation. **Jinbiao Huang:** Validation, Data curation. **Wei Li:** Data curation. **Xiangyang Yu:** Validation, Methodology, Data curation. **Jiang Ma:** Writing – review & editing, Validation, Supervision, Resources, Investigation, Funding acquisition. **Yu Zhang:** Methodology, Data curation. **Luyao Li:** Writing – review & editing, Writing – original draft, Validation, Methodology, Investigation, Formal analysis, Data curation, Conceptualization. **Jiasen Sun:** Data curation. **Chenchen Yuan:** Writing – review & editing, Supervision, Formal analysis. **Kangyu Lin:** Validation, Methodology.

Declaration of Competing Interest

The authors declare that they have no known competing financial interests or personal relationships that could have appeared to influence the work reported in this paper.

Acknowledgment

The work was financially supported by the Science and Technology Innovation Commission Shenzhen (Grants No. RCJC20221008092730037 and 20220804091920001), the Key-Area Research and Development Program of Guangdong Province (Grant No. 2024B0101070001), the Research Team Cultivation Program of Shenzhen University (Grant No. 2023QNT001). This work was also supported by the National Natural Science Foundation of China (Grant No. 52071078). We thank the Instrumental Analysis Center of Shenzhen University for the assistance with the electron microscope.

Appendix A. Supporting information

Supplementary data associated with this article can be found in the online version at doi:10.1016/j.jmatprotec.2025.119178.

Data availability

All data needed to evaluate the conclusions in the paper are present in the paper and/or the supplementary information. Data are also available from the corresponding author upon request.

Angelo P.C., Powder metallurgy: science, technology and applications, PHI Learning Pvt. Ltd., Delhi, 2022.

References

[1] Callister, W.D., Rethwisch, D.G., 1991. Materials science and engineering: an introduction. Mater. Des. 12, 59. https://doi.org/10.1016/0261-3069(91)90101-9.

[2] Saito, T., Oaki, Y., Nishimura, T., Isogai, A., Kato, T., 2014. Bioinspired stiff and flexible composites of nanocellulose-reinforced amorphous $CaCO_3$. Mater. Horiz. 1 (3), 321–325. https://doi.org/10.1039/c3mh00134b.

[3] Lubin, G., 2013. Handbook of composites. Van Nostrand Reinhold Company Inc, New York.

[4] Sajan, S., Selvaraj, D.P., 2021. A review on polymer matrix composite materials and their applications. Mater. Today. Proc. 47, 5493–5498. https://doi.org/10.1016/j.matpr.2021.08.034.

[5] Donald, I.W., McMillan, P.W., 1976. Ceramic-matrix composites. J. Mater. Sci. 11 (5), 949–972. https://doi.org/10.1007/BF00542312.

[6] Krishna, M.G., Kumar, K.P., Swapna, M.N., Rao, J.B., Bhargava, N., 2017. Metal-metal composites-an innovative way for multiple strengthening. Mater. Today. Proc. 4 (8), 8085–8095. https://doi.org/10.1016/j.matpr.2017.07.148.

[7] Wejrzanowski, T., Grybczuk, M., Chmielewski, M., Pietrzak, K., Kurzydlowski, K.J., Strojny-Nedza, A., 2016. Thermal conductivity of metal-graphene composites. Mater. Des. 99, 163–173. https://doi.org/10.1016/j.matdes.2016.03.069.

[8] Nakagawa, N., Ohtsubo, H., Mitani, A., Shimizu, K., Waku, Y., 2005. High temperature strength and thermal stability for melt growth composite. J. Eur. Ceram. Soc. 25 (8), 1251–1257. https://doi.org/10.1016/j.jeurceramsoc.2005.01.030.

[9] Hashim, J., Looney, L., Hashmi, M.S.J., 1999. Metal matrix composites: production by the stir casting method. J. Mater. Process. Technol. 92, 1–7. https://doi.org/10.1016/S0924-0136(99)00118-1.

[10] Contreras, A., Lopez, V.H., Bedolla, E., 2004. Mg/TiC composites manufactured by pressureless melt infiltration. Scr. Mater. 51 (3), 249–253. https://doi.org/10.1016/j.scriptamat.2004.04.007.

[11] Park, J.-H., Hagio, T., Ichino, R., 2023. Improvement in the corrosion resistance of electrodeposited Ni-W alloy by MWCNT co-deposition and prevention of metal-carbon interfacial corrosion by carbide formation. J. Alloy. Compd. 939, 168788. https://doi.org/10.1016/j.jallcom.2023.168788.

[12] Angelo, P.C., 2022. Powder metallurgy: Science, technology and applications. PHI Learning Pvt. Ltd, Delhi.

[13] Zhang, X.P., Ye, L., Mai, Y.W., Quan, G.F., Wei, W., 1999. Investigation on diffusion bonding characteristics of SiC particulate reinforced aluminium metal matrix composites (Al/SiCp-MMC). Compos. Part A 30 (12), 1415–1421. https://doi.org/10.1016/s1359-835x(99)00040-8.

[14] Wang, X.J., Hu, X.S., Wu, K., Zheng, M.Y., Zheng, L., Zhai, Q.J., 2009. The interfacial characteristic of SiCp/AZ91 magnesium matrix composites fabricated by stir casting. J. Mater. Sci. 44, 2759–2764. https://doi.org/10.1007/s10853-009-3360-8.

[15] Mahamood, R.M., 2017. Laser metal deposition process of metals, alloys, and composite materials. Springer, Cham.

[16] Sharifi, E.M., Karimzadeh, F., 2011. Wear behavior of aluminum matrix hybrid nanocomposites fabricated by powder metallurgy. Wear 271 (7), 1072–1079. https://doi.org/10.1016/j.wear.2011.05.015.

[17] Jenkins, I., 1964. Some aspects of residual porosity in powder metallurgy. Powder Met. 7 (13), 68–93. https://doi.org/10.1179/pom.1964.7.13.006.

[18] Pan, J., Ivanov, Y.P., Zhou, W.H., Li, Y., Greer, A.L., 2020. Strain-hardening and suppression of shear-banding in rejuvenated bulk metallic glass. Nature 578 (7796), 559–562. https://doi.org/10.1038/s41586-020-2016-3.

[19] Tian, L., Cheng, Y.-Q., Shan, Z.-W., Li, J., Wang, C.-C., Han, X.-D., Sun, J., Ma, E., 2012. Approaching the ideal elastic limit of metallic glasses. Nat. Commun. 3 (1), 609. https://doi.org/10.1038/ncomms1619.

[20] Li, Y.-C., Zhang, C., Xing, W., Guo, S.-F., Liu, L., 2018. Design of Fe-based bulk metallic glasses with improved wear resistance. ACS Appl. Mater. Interfaces 10 (49), 43144–43155. https://doi.org/10.1021/acsami.8b11561.

[21] Li, X., Zhou, J., Shen, L., Sun, B., Bai, H., Wang, W., 2023. Exceptionally high saturation magnetic flux density and ultralow coercivity via an amorphous–nanocrystalline transitional microstructure in an FeCo-based alloy. Adv. Mater. 35 (50), 2205863. https://doi.org/10.1002/adma.202205863.

[22] Liang, S.X., Jia, Z., Liu, Y.J., Zhang, W., Wang, W., Lu, J., Zhang, L.C., 2018. Compelling rejuvenated catalytic performance in metallic glasses. Adv. Mater. 30 (45), 1802764. https://doi.org/10.1002/adma.201802764.

[23] Wang, X., Yang, C., Fan, C., Liu, R., Sun, L., Zhang, J., Zhan, Z., Wang, W., 2004. Effect of proton irradiation on structure relaxation of $Zr_{41.5}Ti_{14.9}Cu_{12.6}Ni_{10.5}Be_{20.4}$ bulk metallic glass. Chin. Sci. Bull. 49, 999–1001. https://doi.org/10.1007/BF03184026.

[24] Ketov, S.V., Sun, Y.H., Nachum, S., Lu, Z., Checchi, A., Beraldin, A.R., Bai, H.Y., Wang, W.H., Louzguine-Luzgin, D.V., Carpenter, M., 2015. Rejuvenation of metallic glasses by non-affine thermal strain. Nature 524 (7564), 200–203. https://doi.org/10.1038/nature14674.

[25] Pang, S.J., Zhang, T., Asami, K., Inoue, A., 2002. Synthesis of Fe–Cr–Mo–C–B–P bulk metallic glasses with high corrosion resistance. Acta Mater. 50 (3), 489–497. https://doi.org/10.1016/S1359-6454(01)00366-4.

[26] Li, X., Wei, D., Zhang, J.Y., Liu, X.D., Li, Z., Wang, T.Y., He, Q.F., Wang, Y.J., Ma, J., Wang, W.H., Yang, Y., 2020. Ultrasonic plasticity of metallic glass near room temperature. Appl. Mater. Today 21, 100866. https://doi.org/10.1016/j.apmt.2020.100866.

[27] Li, L., Li, X., Huang, Z., Huang, J., Liu, Z., Fu, J., Wen, W., Zhang, Y., Huang, S., Ren, S., Ma, J., 2023. Joining of metallic glasses in liquid via ultrasonic vibrations. Nat. Commun. 14 (1), 6305. https://doi.org/10.1038/s41467-023-42014-x.

[28] Upadhyaya, G.S., 1997. Powder metallurgy technology. Cambridge Int Science Publishing, Cambridge.

[29] Chen, W., Liu, Z., Schroers, J., 2014. Joining of bulk metallic glasses in air. Acta Mater. 62, 49–57. https://doi.org/10.1016/j.actamat.2013.08.053.

[30] Cai, H., Zhang, M., Shi, J., Zhang, J., Ma, Y., Deng, B., Gong, P., Deng, L., Jin, J., Tang, X., Wang, X., 2025. Enhancing rejuvenation of metallic glass via vibration-superimposed elastic loads. Int. J. Mech. Sci. 295, 110285. https://doi.org/10.1016/j.ijmecsci.2025.110285.

[31] Sun, F., Wang, B., Luo, F., Yan, Y.Q., Ke, H.B., Ma, J., Shen, J., Wang, W.H., 2020. Shear punching of bulk metallic glasses under low stress. Mater. Des. 190, 108595. https://doi.org/10.1016/j.matdes.2020.108595.

[32] Wang, Y.-J., Jiang, M.Q., Tian, Z.L., Dai, L.H., 2016. Direct atomic-scale evidence for shear–dilatation correlation in metallic glasses. Scr. Mater. 112, 37–41. https://doi.org/10.1016/j.scriptamat.2015.09.005.

[33] Galindo-Torres, S.A., Zhang, X., Krabbenhoft, K., 2018. Micromechanics of Liquefaction in Granular Materials. Phys. Rev. Appl. 10 (6), 064017. https://doi.org/10.1103/PhysRevApplied.10.064017.

[34] Murali, P., Ramamurty, U., 2005. Embrittlement of a bulk metallic glass due to sub-Tg annealing. Acta Mater. 53 (5), 1467–1478. https://doi.org/10.1016/j.actamat.2004.11.040.

[35] Shiue, S.-T., Shen, T.-Y., 2005. Effect of thermal stresses on the static fatigue of double-coated optical fibers. Mater. Chem. Phys. 89 (1), 159–163. https://doi.org/10.1016/j.matchemphys.2004.08.030.

[36] Ma, J., Yang, C., Liu, X., Shang, B., He, Q., Li, F., Wang, T., Wei, D., Liang, X., Wu, X., Wang, Y., Gong, F., Guan, P., Wang, W., Yang, Y., 2019. Fast surface dynamics enabled cold joining of metallic glasses. Sci. Adv. 5 (11), eaax7256. https://doi.org/10.1126/sciadv.aax7256.

[37] Li, L., Wen, W., Huang, J., Fu, J., Ma, J., 2022. Rapid fabrication of ultra-fine grain intermetallic compound powder in milliseconds under ultrasonic vibrations. Intermetallics 149, 107672. https://doi.org/10.1016/j.intermet.2022.107672.

[38] Komarov, S.V., Kuwabara, M., Abramov, O.V., 2005. High power ultrasonics in pyrometallurgy: current status and recent development. ISIJ Int 45 (12), 1765–1782. https://doi.org/10.2355/isijinternational.45.1765.

[39] Wu, W.-H., Zhai, W., Hu, H.-B., Wei, B.-B., 2017. Acoustic field and convection pattern within liquid material during ultrasonic processing. Acta Phys. Sin. 66 (19), 194303. https://doi.org/10.7498/aps.66.194303.

[40] Chini, G.P., Malecha, Z., Dreeben, T.D., 2014. Large-amplitude acoustic streaming. J. Fluid Mech. 744, 329–351. https://doi.org/10.7498/aps.66.194303.

[41] Busch, R., 2000. The thermophysical properties of bulk metallic glass-forming liquids. Jom 52, 39–42. https://doi.org/10.1007/s11837-000-0160-7.

[42] Wang, Y., Fan, F., Agapov, A.L., Saito, T., Yang, J., Yu, X., Hong, K., Mays, J., Sokolov, A.P., 2014. Examination of the fundamental relation between ionic transport and segmental relaxation in polymer electrolytes. Polymer 55 (16), 4067–4076. https://doi.org/10.1016/j.polymer.2014.06.085.

[43] Peng, Q., Xie, Y., Zhu, B., Chen, W., Schroers, J., Chen, M., Liu, Z., 2020. Joining mechanism of bulk metallic glasses in their supercooled liquid region. J. Mater. Process. Technol. 279, 116583. https://doi.org/10.1016/j.jmatprotec.2019.116583.

[44] Wang, W.H., 2012. The elastic properties, elastic models and elastic perspectives of metallic glasses. Prog. Mater. Sci. 57 (3), 487–656. https://doi.org/10.1016/j.pmatsci.2011.07.001.

[45] Legros, M., Dehm, G., Arzt, E., Balk, T.J., 2008. Observation of giant diffusivity along dislocation cores. Science 319 (5870), 1646–1649. https://doi.org/10.1126/science.1151771.

[46] Langenecker, B., 1966. Effects of ultrasound on deformation characteristics of metals. IEEE Trans. Sonics Ultrason 13 (1), 1–8. https://doi.org/10.1109/T-SU.1966.29367.

[47] Shi, J., Zhang, M., Li, Q., Cai, H., Zhang, J., Liu, J., Deng, L., Jin, J., Gong, P., Tang, X., Deng, B., Wang, X., 2025. Influences of ultrasonic vibration on the microstructure evolution of pure aluminum during uniaxial compression. J. Alloy. Compd. 1020, 179430. https://doi.org/10.1016/j.jallcom.2025.179430.